Pergamon

Int. J. Solids Structures Vol. 35, Nos. 3–4, pp. 239–267, 1998

0020–7683/98 $19.00 + .00

PII: S0020–7683(97)00062–0

IN-PLANE CRUSHING OF A POLYCARBONATE HONEYCOMB

SCOTT D. PAPKA and STELIOS KYRIAKIDES
Research Center for Mechanics of Solids, Structures & Materials, The University of Texas at Austin, WRW 110, Austin, TX 78712-1085, U.S.A.

(*Received* 10 *October* 1996; *in revised form* 23 *January* 1997)

Abstract—The in-plane compressive response and crushing of a polycarbonate honeycomb with circular close-packed cells is studied through combined experimental and analytical efforts. Under displacement controlled quasi-static loading the response is characterized by a relatively sharp rise to a load maximum followed by a drop down to an extended load plateau which is then terminated by a sharp rise in load. In the initial rising part of the response, the deformation is essentially uniform throughout the specimen. Following the load maximum, the deformation localizes in a narrow zone of cells. These cells collapse in a shear-type mode until contact between cell walls arrests their deformation and causes spreading of the deformation to the neighboring rows of cells where the process is repeated. This propagation of the collapsed zone occurs at a relatively constant load and continues until all the rows of cells have collapsed. As a result of the rate dependence of the material, the initiation and propagation stresses increase as the rate of crushing of the honeycomb is increased. This process of crushing has been simulated numerically using appropriately nonlinear kinematics. An elastic-powerlaw viscoplastic constitutive rule, calibrated to uniaxial experiments spanning strain rates of six decades, is used to model the behavior of the polycarbonate. In addition, the model is capable of treating contact between cell walls which result from crushing. Results from analyses involving a characteristic cell and from full scale simulations of the experiments are presented which are shown to be in excellent agreement with the experimental results. © Elsevier Science Ltd.

1. INTRODUCTION

Honeycombs have been widely used as models for studying the mechanical properties of cellular materials [e.g. Shaw and Sata (1966); Patel and Finnie (1970); Gibson *et al.* (1982); Ashby (1983); Gibson and Ashby (1988); Klintworth and Stronge (1988); Zhang and Ashby (1992); Warren and Kraynik (1987); Warren *et al.* (1989); Papka and Kyriakides (1994); Prakash *et al.* (1996); Triantafyllidis and Schraard (1997)]. Their regularity and periodicity lends itself to systematic analysis of the mechanisms governing the compressive response and crushing of cellular materials. In a preceding publication (1994) we used aluminum honeycombs with approximately hexagonal cells to illustrate that the compressive response along the ribbon direction is governed by an instability with a shear-type mode. The onset of this mode of deformation causes localized deformation to a narrow zone involving a few rows of cells. Subsequent displacement-controlled compression results in spreading of the collapse throughout the material while the average stress remains at a relative stress plateau. The stress plateau is terminated when all the cells have collapsed and the now densified material recovers significant stiffness.

The problem is governed by nonlinearities in geometry and contact between the cell walls and by material nonlinearity due to the elastoplastic characteristics of the aluminum. It was demonstrated that with proper modeling of these nonlinearities, all aspects of this behavior could be simulated numerically and that the key honeycomb properties (elastic modulus, stress at onset of crushing, plateau stress and densification strain) could be calculated with engineering accuracy from the response of a representative micromodel (local response) as well as from full scale simulations.

Many of the so-called "rigid" foams, widely used in engineering practice, are made from polymers. As a result, in addition to the factors listed above, their mechanical properties are also affected by the rate of loading [e.g. Shaw and Sata (1966); Green *et al.* (1969); Hinkley and Yang (1975); Richardson and Nandra (1985); Sherwood and Frost

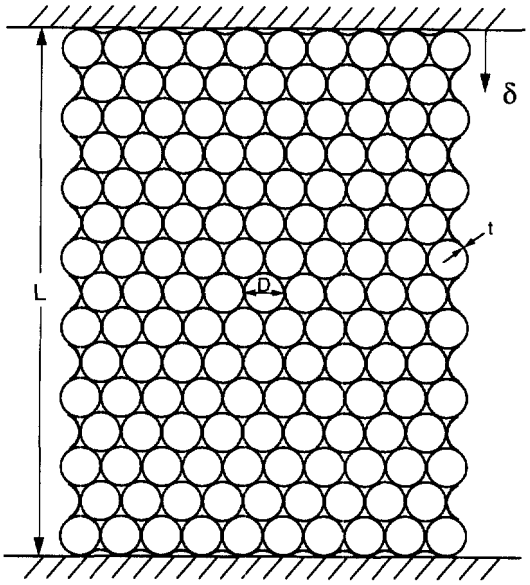

Fig. 1. Geometry of honeycomb specimens used in the experiments and in the analysis.

(1991); Shim *et al.* (1992)]. In the case of closed cell foams the exhibited rate dependence, especially at higher deformation rates corresponding to impact, is partly due to the escaping of the gas inside the cells. At lower deformation rates [Richardson and Nandra (1985); Sherwood and Frost (1991)], the inherent rate sensitivity of polymeric materials is the major contributor to the rate sensitivity of the foams. This is also the case for open cell polymeric foams.

In this study we use a polymeric (polycarbonate) honeycomb with circular cells as a model material to study the compressive response and crushing behavior of rate-dependent cellular materials. The study involves combined experimental and analytical efforts and follows very much the work style established in Papka and Kyriakides (1994).

2. HONEYCOMB CRUSHING EXPERIMENTS

The honeycomb used in the experiments had circular cells in a hexagonal close packed arrangement (see Fig. 1, manufactured by Plascore). The honeycomb is made from polycarbonate extruded tubes with diameter (D) of 0.274 in (6.96 mm) and an average wall thickness (t) of 5.68×10^{-3} in (144 μm). The tubes are bonded to each other to form a honeycomb 13 in (330 mm) thick (typical size 4×8 ft—1.22×2.44 m). The thick block is then sliced to form honeycomb plates of the required thickness (in our case 1.25 in—32 mm). The density of the polycarbonate (ρ) is 74.4 lb ft^{-3} (1191 kg m^{-3}). The density (ρ^*) of such a honeycomb with a perfect geometry is given approximately by

$$\rho^* = \frac{2\pi}{\sqrt{3}} \rho \left(\frac{t}{D}\right). \tag{1}$$

For the present material, (1) yields a relative density (ρ^*/ρ) of 7.5% which compares with the measured value of 7.06% ($\rho^* = 5.25$ lb ft^{-3}—84.1 kg m^{-3}).

The specimens used in the crushing experiments were cut from the 1.25 in thick honeycomb plate and had typical dimensions of 15 rows by 10 columns of cells as shown in Fig. 1. The ends of the specimens were carefully cleaned to minimize friction effects. They were crushed between two parallel polished steel plates, mounted onto standard universal testing machines. The crushing was conducted at chosen constant end-displacement rates ($\dot{\delta}$). The load and end displacement were recorded by a data acquisition system on a common time base. Full field views of the deformation of the specimen were

recorded by a video system which was synchronized with the data acquisition system. Crushing experiments were conducted at normalized displacement rates ($\dot{\delta}/L$) which ranged from 5×10^{-5} to 2×10^{0}. The effect of specimen size on the recorded response was studied in separate experiments.

2.1. *Discussion of a typical honeycomb crushing experiment*

The compressive response of such a honeycomb crushed at a normalized displacement rate of 5×10^{-3} s^{-1} is shown in Fig. 2(a) ($\dot{\delta}/L$ will be called 'strain' rate). The ratio of the applied load and the initial cross-sectional area, called stress (σ), is plotted against the applied displacement (δ) normalized by the undeformed height of the specimen ($L \approx 3.7$ in—94 mm). A sequence of pictures of the deformed honeycomb corresponding to the equilibrium states identified by (•) on this response is shown in Fig. 2(b). The response has the general features common to cellular materials [e.g. see Gibson and Ashby (1982, 1988)]. Initially, it is relatively stiff and nearly linear. Each cell deforms symmetrically about a vertical axis passing through its center and deformation is essentially uniform throughout the specimen [see configuration ① in Fig. 2(b)]. At a stress of approximately 7 psi (48 kPa), the response starts to soften and eventually a limit load develops at a stress of $\sigma_I = 8.6$ psi (59 kPa) and a strain of $\varepsilon_I = 7.2\%$ (the suffix I stands for *initiation*). Beyond the limit load, deformation localizes to a narrow, horizontal zone involving cell rows 11 and 12. The deformation of the cells in these rows has now switched to an unsymmetric, shear-type mode. At the same time, cells outside this zone, near the top of the specimen, remain symmetrically deformed. As the collapse of the two rows progresses, deformation spreads to the two neighboring rows. Local deformation in rows 11 and 12 is arrested when the walls of the two rows come into contact which corresponds to a local minimum in the response.

Although the neighboring rows of cells have been weakened by the collapse of rows 11 and 12, a small additional effort, corresponding to the first upturn in the response, is required to collapse them. Essentially the process repeats itself creating the stress plateau with undulations seen in Fig. 2(a) except that the second and subsequent stress humps stay, in general, below the level of the initiation stress. Configurations ④–⑥ show the propagation of the collapsed region through the specimen. Eventually, all the cells collapse except for a few next to the loading plates which remained relatively stiff due to constraint provided by the plates (configuration ⑦). The specimen then regains its stability and the load increases sharply (densification). [The events described here are very similar to those reported in Papka and Kyriakides (1994) for aluminum hexagonal honeycombs loaded in a similar fashion although the more regular geometry of the present honeycomb results in a cleaner experiment. Some similarities also exist with the observations of Shim and Stronge (1986) in crushing experiments involving a close packed array of circular metallic tubes (not bonded) confined between rigid side walls].

The propagation of collapse involves the same shear-type mode which causes the initial instability. Figure 3 shows close-up views of a characteristic cell in the process of collapsing. The undeformed configuration is identified as ⓤ. In configuration ①, the cell deforms symmetrically while in configuration ② the onset of unsymmetric deformation is observed. Configurations ③ and ④ show the cell at increasing stages of collapse while in ⑤ the cell walls come into contact arresting further local deformation.

Although not obvious from Fig. 2(b), the video recording clearly showed that the propagating front of collapse involved two, usually adjoining, rows of cells. Furthermore, each stress undulation corresponds to the collapse of such pairs of rows. Thus, the response of specimens of this height were characterized by seven stress hills and valleys. This order of events can get somewhat disrupted depending on the position of the initiation of collapse and by local imperfections. In this particular case, the stress plateau extends to 70% of the original height of the specimen. The average value of the stress plateau, which will be called *propagaton stress* (σ_P), is 8.0 psi (55 kPa) and the amplitude of the stress undulations ($\Delta\sigma_a$) is 0.52 psi (3.6 kPa—mean value). The range and average values of the major material properties measured in five such experiments are listed in Table 1 ($\Delta\varepsilon_P$ is the difference between the value of average strain (δ/L) at which densification starts and the initiation

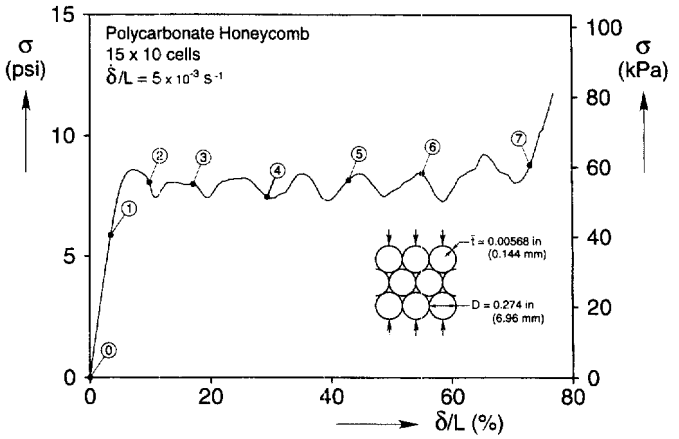

Fig. 2. (a) Recorded force–displacement crushing response of polycarbonate honeycomb.

strain). The repeatability of these values from experiment to experiment was excellent. $\Delta\sigma_a$ exhibited the largest variation probably due again to variation in cell ovalization, in bond length, and other geometric imperfections.

The elastic modulus of the honeycomb (E^*) was measured in special experiments in which a 2-in gage length extensometer was mounted onto the honeycomb specimen at mid-height in order to negate the influence of the ends of the specimens. The elastic modulus measured at this strain rate was 237 psi (1.63 MPa). The variation in the measured modulus from four experiments was 235–239 psi (1.62–1.65 MPa).

2.2. *Effect of rate of crushing*

Polycarbonate is a rate dependent material (see the next section) and, thus, it was desirable to also establish the effect of rate on the crushing response to our honeycomb. To this end, experiments similar to the one described above were conducted at six different end-displacement rates in the range of $5 \times 10^{-5} \leqslant \dot{\delta}/L \leqslant 2 \times 10^{0}$.

The effect of rate on the crushing responses is illustrated in Fig. 4 where the response presented in Fig. 2(a) is compared with one from a specimen crushed at a displacement rate two decades higher and a second crushed at a rate of two decades lower. The initial elastic parts of the three responses are essentially indistinguishable in the scale of the figure (elastic moduli measured in independent experiments are listed in Table 1). However, the responses begin to differ soon after each becomes nonlinear. The limit stresses and plateau stresses increase with rate. The average values of σ_P for the three tests in this figure are 7.5, 8.0 and 8.5 psi (52, 55 and 59 kPa). Interestingly, both the number and location of the undulations remain nearly the same although their amplitude decreases as the strain rate increases (differences in the horizontal positions in Fig. 4 of some of the undulations are primarily due to differences in the vertical position in the specimens of the site of initiation of the instability). The mean values of the amplitudes of the undulations in the two new responses are 0.52 psi (3.6 kPa) for the lower rate one, and 0.31 psi (2.1 kPa) for the one tested at the faster rate (see also mean values of $\Delta\sigma_a$ from several experiments listed in Table 1). The extent of the plateau remains essentially unaffected by rate. It is important to note that after the onset of localization, the meaning of strain rate as defined by $\dot{\delta}/L$ ceases to be applicable. The strain rate inside the propagating collapse front is significantly higher than the strain rate experienced during homogeneous deformation, while outside of it deformation essentially ceases. As the front propagates, material points entering it experience first an acceleration in strain rate followed by a deceleration due to the arrest of local deformation. Such local changes in strain rate will require special attention in modeling.

The range and mean values of major parameters of 16 responses of this type are listed in Table 1, categorized according to end-displacement rate. The narrowness of the ranges of the variables E^*, σ_1, σ_P and $\Delta\varepsilon_P$ for each rate attest to the excellent repeatability of the experimental results. The elastic modulus of the material, E^*, is seen to increase slightly

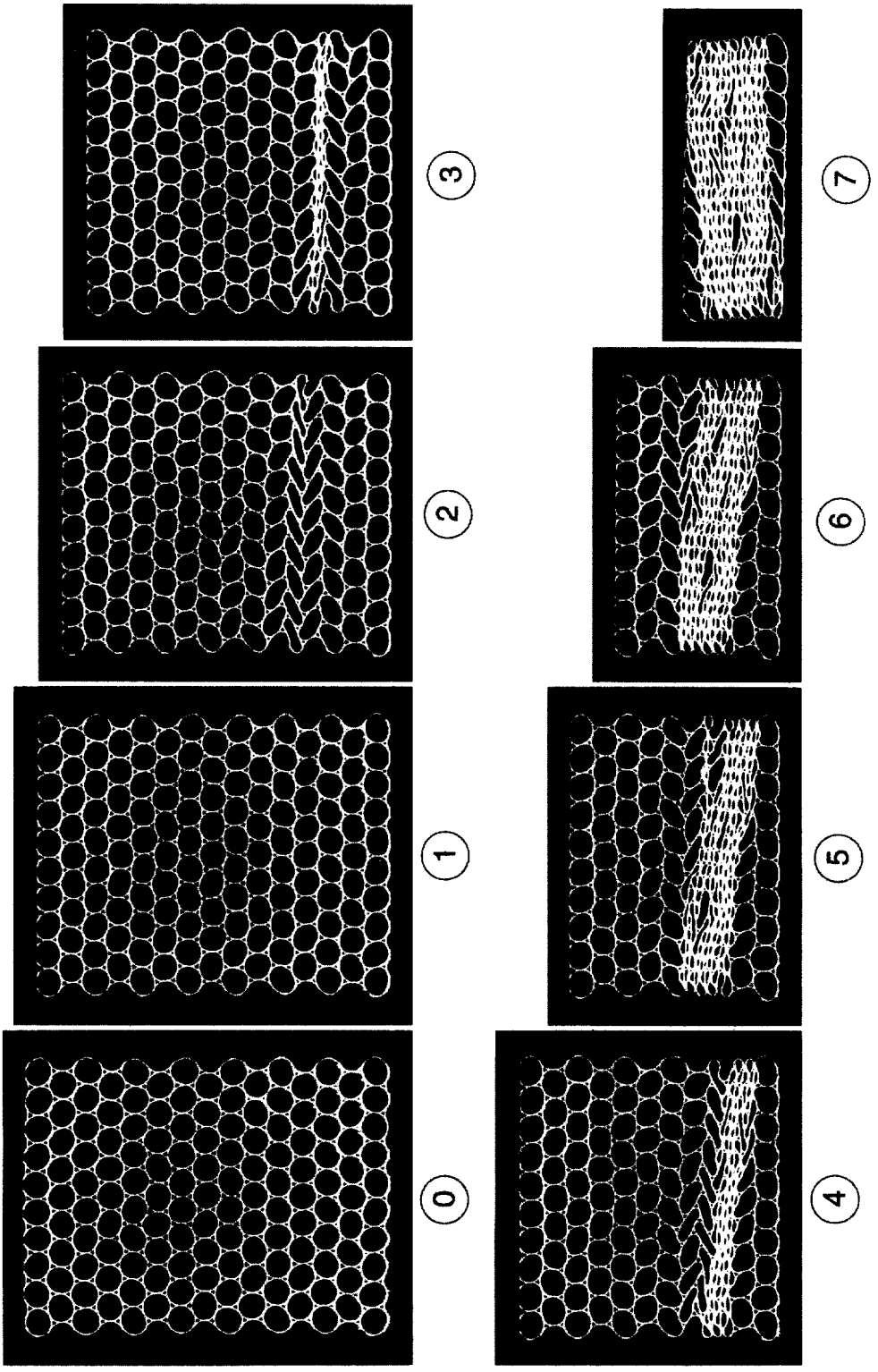

Fig. 2 (b) sequence of deformed configurations corresponding to response in Fig. 2(a).

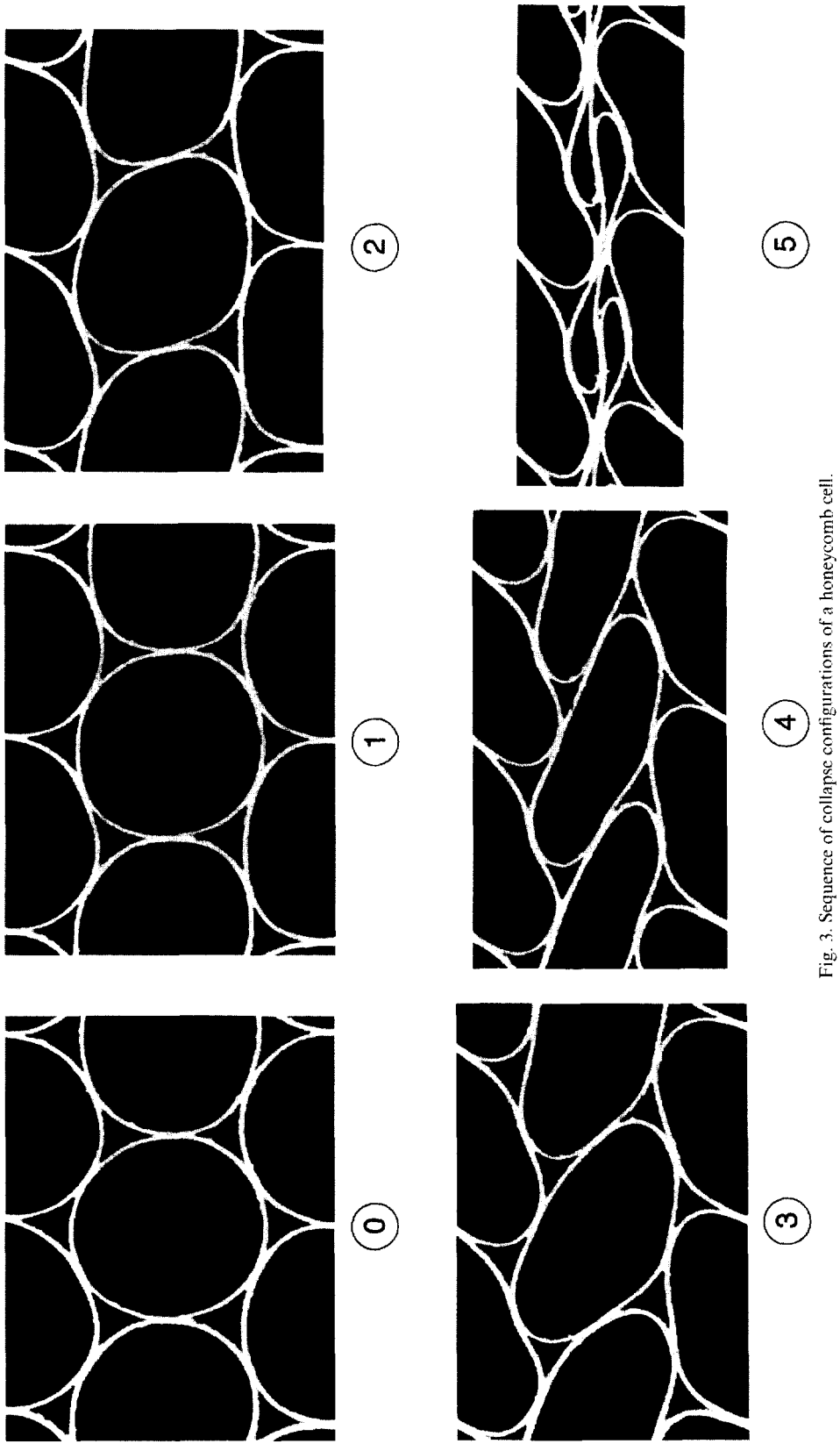

Fig. 3. Sequence of collapse configurations of a honeycomb cell.

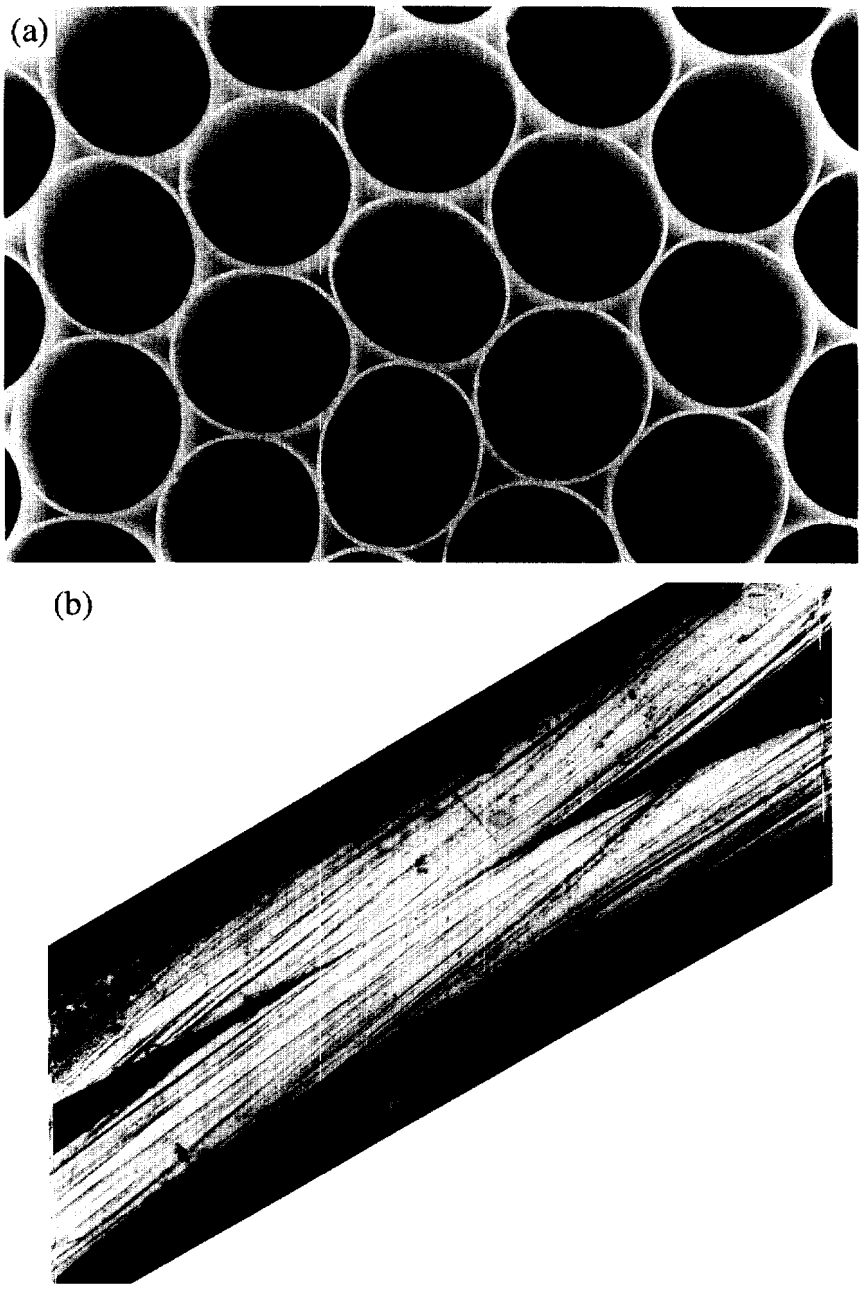

Fig. 8. (a) Photograph of honeycomb showing cell ovalization in a cluster of cells; (b) photomicrograph of cell bond line.

Table 1. Average values and range of elastic moduli, limit stresses, propagation stresses, stress undulation amplitudes and plateau strains from honeycomb crushing experiments

$\dot{\delta}/L$ s^{-1}		E^* psi (MPa)	σ_I psi (kPa)	σ_P psi (kPa)	$\Delta\sigma_a$ psi (kPa)	$\Delta\varepsilon_P$ (%)
5×10^{-5}	Average value	233 (1.61)	8.63 (59.5)	7.50 (51.7)	0.60 (4.1)	61.6
	Range	229–237 (1.58–1.63)	8.63 (59.5)	7.46–7.53 (51.4–51.9)	0.52–0.68 (3.6–4.7)	61.5–61.6
	No. of spec.	4	2	2	2	2
5×10^{-4}	Average value	236 (1.63)	8.85 (61.0)	7.86 (54.2)	0.47 (3.2)	61.3
	Range	236–237 (1.63)	8.80–8.90 (60.7–61.4)	7.84–7.87 (54.1–54.3)	0.41–0.52 (2.8–3.6)	59.8–62.7
	No. of spec	4	2	2	2	2
5×10^{-3}	Average value	237 (1.63)	8.72 (60.1)	8.06 (55.6)	0.47 (3.2)	62.2
	Range	235–239 (1.62–1.65)	8.51–8.89 (58.7–61.3)	7.90–8.16 (54.5–56.3)	0.32–0.64 (2.2–4.4)	60.1–63.1
	No. of spec.	4	5	5	5	5
5×10^{-2}	Average value	247 (1.70)	9.19 (63.4)	8.51 (58.7)	0.46 (3.2)	61.1
	Range	247–248 (1.70–1.71)	9.11–9.33 (62.8–64.3)	8.42–8.62 (58.1–59.4)	0.44–0.48 (3.0–3.3)	60.7–61.7
	No. of spec.	2	3	3	3	3
5×10^{-1}	Average value	—	9.11 (62.8)	8.63 (59.5)	0.42 (2.9)	63.7
	Range	—	9.04–9.18 (62.3–63.3)	8.54–8.72 (58.9–60.1)	0.31–0.53 (2.1–3.7)	59.6–67.8
	No. of spec.	—	2	2	2	2
2×10^{0}	Average value	—	9.21 (63.5)	8.71 (60.1)	0.33 (2.3)	61.5
	Range	—	9.12–9.30 (62.9–64.1)	8.61–8.81 (59.4–60.7)	0.31–0.34 (2.1–2.3)	58.5–64.4
	No. of spec.	—	2	2	2	2

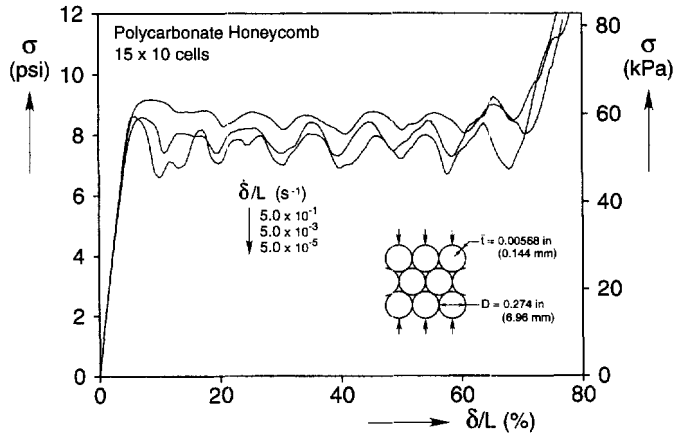

Fig. 4. Comparison of force–displacement compressive responses from three honeycomb specimens loaded at three different end displacement velocities.

with rate while the extent of the stress plateau is essentially unaffected by it. The initiation and propagation stresses from all experiments are plotted against the displacement rate in Fig. 5. The increase of σ_P with rate is well illustrated. The initiation stresses exhibit a larger scatter than σ_P and a milder dependence on rate. It is important to point out that the value of the initiation stress is influenced by geometric imperfections in the honeycomb. By

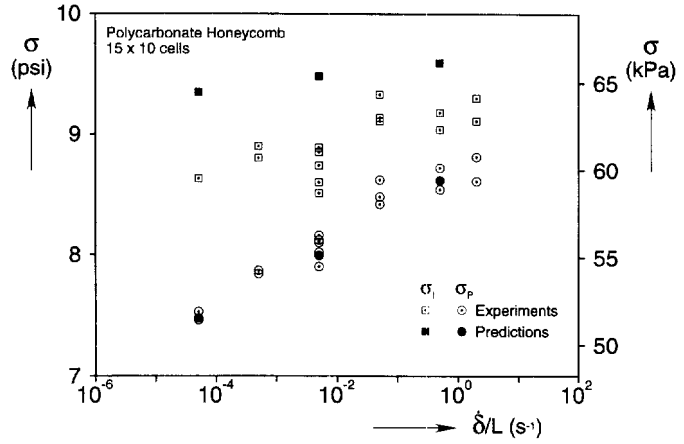

Fig. 5. Summary of experimental and predicted values of initiation and propagation stresses plotted against average strain rate.

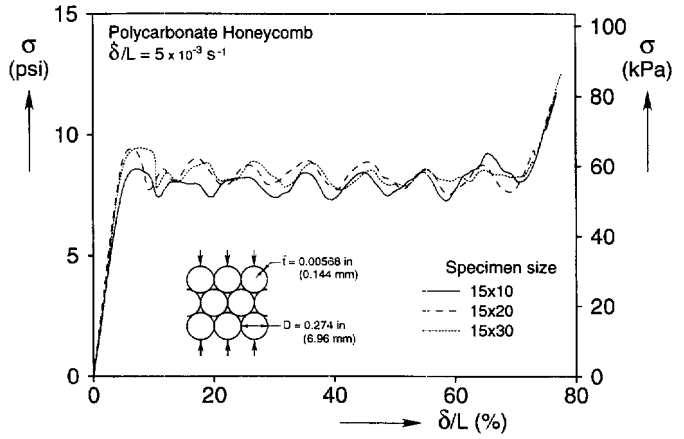

Fig. 6. Comparison of force–displacement compressive responses of honeycomb specimens of three different widths.

contrast, the propagation stress is not significantly affected by such imperfections. The random distribution of geometric imperfections is responsible for the observed scatter in the values of σ_I. The variable exhibiting the largest scatter is $\Delta\sigma_a$ again most probably due to the influence of geometric imperfections. However, the mean values of $\Delta\sigma_a$ are clearly seen to decrease as the rate of crushing is increased.

2.3. *Effect of specimen width*

In experiments of the type reported here, a general requirement is that the specimen dimensions be 'large' compared to the characteristic dimension of the microstructure, which in this case is the cell diameter. Several experiments were conducted to establish the effect of specimen size on the results. Responses from specimens of the same height (15 rows or ~3.7 in—94 mm), but with widths of 10, 20 and 30 columns of cells are compared in Fig. 6. The main features of the three responses are very similar. The stress undulations have the same periods and approximately the same amplitudes and the plateau strains are also the same. Furthermore, the crushing mechanisms were very similar to that in Fig. 2(b). The average values of the propagation stresses are 8.0 psi (55 kPa) for the smaller specimen and 8.3 psi (57 kPa) for the two larger ones. This difference was considered to be acceptably small and the smaller width specimen was adopted in the test program. In addition to savings in material costs, smaller specimens were preferred in order to keep the large scale numerical simulations of the collapse process that follow at a manageable size.

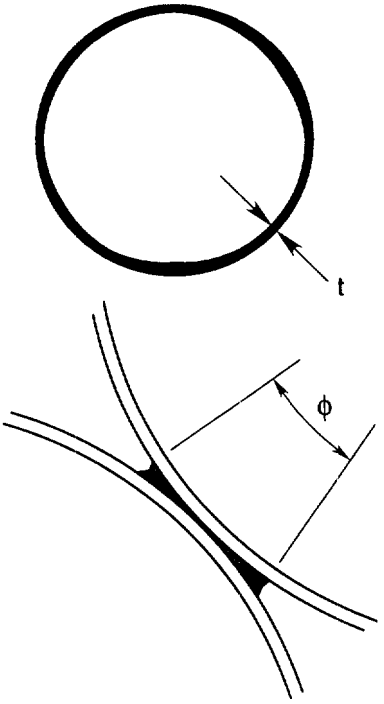

Fig. 7. Geometric details of cells: (a) measured thickness variation in a honeycomb cell (magnified × 5); (b) angular measure of bonded arc.

2.4. *Honeycomb geometry and imperfections*

In the fourth section of this paper we present a numerical model of the crushing of polymeric honeycombs. In order to facilitate a direct comparison of calculated and measured responses, it was essential that we had accurate measures of the geometric characteristics of the honeycomb. Furthermore, a clear picture of the types and extents of any geometric imperfections present in the test specimens was required. The geometry of the honeycomb was analyzed using a microscope and the following characteristics were established:

- The diameters (D) of the cells had a mean value of 0.274 in (6.96 mm) and a standard deviation (SD) of 0.002 in (51 μm).
- The wall thickness of the cells (t) was found to have variations around the circumference. Figure 7(a) shows a view of a typical cell cross-section where the thickness variations were exaggerated (× 5). The mean value of t and the SD of the measurements is given in Table 2.
- The cells were found to be ovalized to varying degrees [see Fig. 8(a)]. The ovalization, defined as

$$\Delta_0 = \frac{D_{\max} - D_{\min}}{D_{\max} + D_{\min}}, \tag{2}$$

was measured for a large number of cells and the mean value and the SD are listed in

Table 2. Geometric characteristics of honeycomb

	D in (mm)	t in (μm)	Δ_0 (%)	ϕ^0
Mean value	0.274 (6.96)	0.00568 (144)	4.88	10.5
SD	0.002 (0.05)	0.00025 (6.4)	1.82	1.9

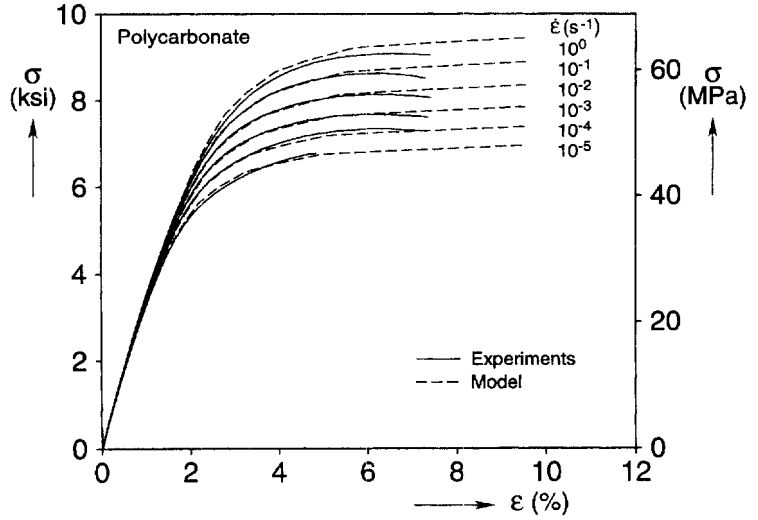

Fig. 9. Experimental stress–strain responses of polycarbonate material and corresponding predictions by the elastic-power law viscoplastic model for strain rates spanning six decades.

Table 2. Although within a local cluster of cells, like the one shown in Fig. 8(a), the principal axes of ovalizations might be related to each other (for compatibility), the orientations of the ovalizations in a larger section of honeycomb were essentially randomly distributed. Such ovalizations also imply small deviations from the perfect closed-packed hexagonal arrangement of the cells.

- Figure 8(b) shows a typical bond between two cells. The bond, which seems to have been formed by a capillary effect, covers a finite arc with an angular span of ϕ° as shown in Fig. 7(b). The average value of this angle and its SD are also listed in Table 2.

3. CHARACTERIZATION AND MODELING OF BASE MATERIAL

The mechanical behavior of the polycarbonate material of the honeycomb was established through a set of uniaxial tension tests on tubes from the same batch as those used to manufacture the honeycomb. The test specimens were typically 11 tube diameters long. Six constant strain rate tests were conducted at rates ranging from 10^0 to 10^{-5} s^{-1}. This range nearly spans the strain rates of the deformations experienced by the honeycomb material in the lateral crushing experiments presented in the previous section. Each test was terminated shortly after the appearance of a neck in the test section of the specimen.

The six stress–strain responses measured are shown in Fig. 9. The initial linear parts of the responses coincide indicating that in this strain rate regime elastic deformations can be considered to be rate independent. By contrast, the subsequent inelastic parts of the responses are seen to exhibit significant rate sensitivity.

This nonlinear material behavior was modeled through the following incremental constitutive model. Strain increments are assumed to consist of an elastic part and an inelastic part

$$\dot{\underline{\varepsilon}} = \dot{\underline{\varepsilon}}^{\mathrm{e}} + \dot{\underline{\varepsilon}}^{\mathrm{p}}. \tag{3}$$

Elastic deformations are linear and isotropic and are related to stresses by

$$\dot{\underline{\varepsilon}}^{\mathrm{e}} = \frac{1+\nu}{E}\dot{\underline{\sigma}} - \frac{\nu}{E}(tr\dot{\underline{\sigma}})\underline{I} \quad \text{or} \quad \dot{\underline{\sigma}} = \underline{C}(E,\nu)\dot{\underline{\varepsilon}}^{\mathrm{e}} \tag{4}$$

where E is the Young's modulus and ν the Poisson's ratio of the material both assumed to be independent of rate (values given in Table 3).

Table 3. Material parameters used in elastic–viscoplastic constitutive model

E ksi (GPa)	ν	σ_0 ksi (MPa)	m	ξ
350 (2.41)	0.3	3.0 (20.7)	0.027	0.25

The inelastic part of the deformation ($\underline{\dot{\varepsilon}}^p$) is assumed to exhibit a simple power law rate dependence [Nadai (1950)], which for a uniaxial state of stress and strain is given by

$$\left(\frac{\dot{\varepsilon}^p}{\dot{\varepsilon}_0}\right)^m = \frac{\sigma}{\Sigma(\varepsilon^p)}. \tag{5}$$

Here, $\dot{\varepsilon}_0$ is a reference strain rate, $\Sigma(\varepsilon^p)$ is the flow stress measured when $\dot{\varepsilon}^p = \dot{\varepsilon}_0$, and m is the rate exponent. In this case, $10^{-3}\ s^{-1}$ was chosen as the reference rate. The yield stress (σ_0) was selected to be 3 ksi (20.7 MPa) and the inelastic part of the response was fitted with a multilinear fit (11 segments of variable strain spans). This fit is drawn with a dashed line in Fig. 9. The value of the rate exponent was found in the usual way to be 0.027. Included in Fig. 9 are the predictions of the stress–strain responses for the other five strain rates using these variables. The results of the model are seen to be in good agreement with the measured responses for all cases up to a stain of approximately 5% when the deformation in the tubes started to become inhomogeneous due to necking (not an issue in the honeycomb where bending deformations are dominant).

The model was generalized to the multiaxial setting through the classical associative plasticity framework [e.g. see Peirce *et al.* (1984)]. The plastic strain rate is given by

$$\underline{\dot{\varepsilon}}^p = \Lambda \frac{\partial f}{\partial \underline{\sigma}} \tag{6}$$

with the following choice for f:

$$f = \sigma_e = \sqrt{\tfrac{3}{2}\underline{s}\cdot\underline{s}}, \quad \underline{s} = \underline{\sigma} - \tfrac{1}{3}(tr\underline{\sigma})\underline{I}. \tag{7}$$

A work compatible measure of equivalent strain is given by

$$\dot{\varepsilon}_e^p = \sqrt{\tfrac{2}{3}\underline{\dot{\varepsilon}}^p \cdot \underline{\dot{\varepsilon}}^p}. \tag{8}$$

Thus, eqns (5), (7) and (8) $\rightarrow$(6) yield

$$\underline{\dot{\varepsilon}}^p = \dot{\varepsilon}_e^p\left(\frac{3}{2}\frac{\underline{s}}{\sigma_e}\right) = \dot{\varepsilon}_0\left(\frac{\sigma_e}{\Sigma(\varepsilon_e^p)}\right)^{1/m}\left(\frac{3}{2}\frac{\underline{s}}{\sigma_e}\right) \tag{9}$$

where

$$\varepsilon_e^p = \int_0^t \dot{\varepsilon}_e^p \, dt. \tag{10}$$

By combining eqns (4) and (9) through eqn (3) and inverting we arrive at

$$\underline{\dot{\sigma}} = \underline{C}\underline{\dot{\varepsilon}} - \left(\frac{3\dot{\varepsilon}_e^p}{2\sigma_e}\right)\underline{C}\underline{s}. \tag{11}$$

In the previous section we saw that in constant end velocity crushing experiments, the honeycomb initially experienced nearly uniform deformation, which was terminated at the first limit load. Following this, deformation localized to a narrow zone and, subsequently, the specimen deformed by progressive collapse of narrow zones of the material. Thus, at the onset of localization, material points away from the deforming zone experience a reduction in rate of deformation and some unloading while those inside the zone experience an increase in rate. During the stress plateau, as particular material points enter the crushing front, they experience an increase in strain rate. Subsequently, as local deformation gets arrested the strain rate decreases.

Several additional uniaxial experiments were conducted in order to establish the material behavior to changes in strain rate. Figure 10 shows a sample of such stress–strain responses. In Fig. 10(a) the specimen was pulled at $\dot{\varepsilon} = 10^{-4}\,s^{-1}$ to a strain of approximately 3% and subsequently the rate was increased by two decades. With the increase in rate the response hardened and smoothly approached that corresponding to the higher rate. By contrast, in Fig. 10(b) the first part of the test was at a rate of $10^{-2}\,s^{-1}$ and the second part at a rate two decades lower. When the rate changed the stress decreased almost in a stepwise fashion until the response at the lower rate was intercepted and was followed thereafter. At a strain of approximately 5%, the specimen was unloaded and reloaded. In Fig. 10(c) following initial loading to a strain of 3% at $\dot{\varepsilon} = 10^{-4}\,s^{-1}$, some unloading was allowed followed by reloading at a rate two decades higher. At a strain of approximately 5%, the specimen was unloaded and then reloaded at the original strain rate.

For numerical expediency, when implementing the model to complex loading histories, like those in Fig. 10, the value of $\dot{\varepsilon}_e^p$ in a given time increment (Δt) was evaluated through the forward gradient method of Peirce *et al.* (1984). This method linearly interpolates the values of $\dot{\varepsilon}_e^p$ at t and $t+\Delta t$ as follows:

$$\frac{\Delta\varepsilon_e^p}{\Delta t} = [(1-\xi)\dot{\varepsilon}_e^p|_t + \xi\dot{\varepsilon}_e^p|_{t+\Delta t}] \tag{12a}$$

where ξ is a numerical parameter selected for optimum performance and

$$\dot{\varepsilon}_e^p|_{t+\Delta t} = \dot{\varepsilon}_e^p|_t + \frac{\partial\dot{\varepsilon}_e^p}{\partial\sigma_e}\Delta\sigma_e + \frac{\partial\dot{\varepsilon}_e^p}{\partial\varepsilon_e^p}\Delta\varepsilon_e^p. \tag{12b}$$

In the present problem, $\xi = 0.25$ was found to yield optimum results. Included in Fig. 10 are the numerical simulations of the three variable rate tests. The model is seen to be able to capture well the transients introduced by the instantaneous switching in rates. We note that modeling of polymeric inelastic behavior through powerlaw viscoplasticity is not very common [although Tugcu and Neale (1987, 1988) successfully used finite deformation versions of such models to model neck propagation in polymeric rods and membranes]. However, the success of the model adopted here to reproduce complex loading histories representative of those seen in the honeycomb confirms that for the time scales of the events in the crushing experiments ($\sim$100 ms to 5 h) this is a viable model.

4. ANALYSIS

In addition to the material nonlinearity discussed above, the problem is characterized by nonlinearities in geometry and contact. In order to treat these nonlinearities accurately,

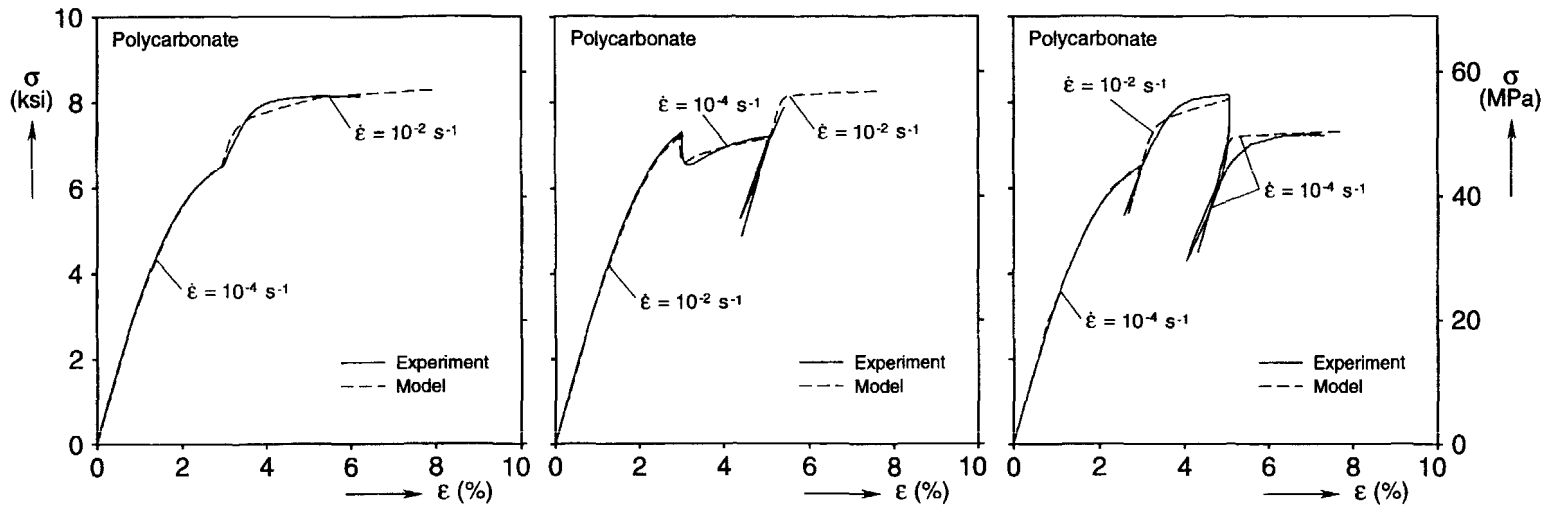

Fig. 10. Experimental and predicted uniaxial stress–strain responses for three different loading histories: (a) strain rate increased by two decades at 3% strain; (b) strain rate decreased by two decades at 3% strain followed by unloading and reloading at a higher rate; (c) strain rate increased and then decreased at various stages of response.

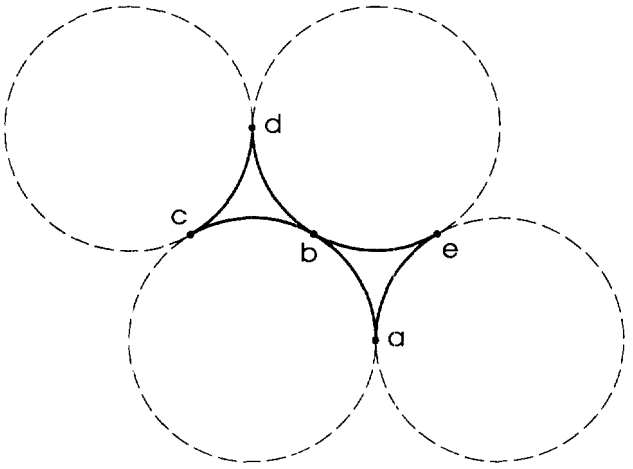

Fig. 11. Geometry of microsection used in numerical analysis.

the problem was discretized using quadratic beam elements (ABAQUS†) based on non-linear kinematics which allow for finite rotations and finite membrane strains. Because the out-of-plane thickness of the honeycomb was approximately five times the cell diameter, the elements were modified so that the deformation of the tubular cells was cylindrical (approximately). The bonded arcs of the cells were modeled by connecting nodes on either side of the bond with rigid beam elements. Typically each cell was modelled by 24 unevenly distributed elements. The distribution of elements around the circumference of the cells was chosen such that the extent of the bond line could be modeled accurately. Each element had two integration points along the length and nine through the thickness. Contact between the walls of crushed cells was modeled by predefining each pair of contact surfaces. ABAQUS then generates the contact elements automatically. This option also allows for finite sliding between the contacting surfaces. The performance of the algorithm was optimized by introducing a mild 'softening' of the contact in the usual fashion.

The cells were assumed to be circular and to be arranged in an hexagonal array. The geometric parameters of the honeycomb (D, t and ϕ) were chosen to correspond to the mean of the measured values listed in Table 2. Geometric imperfections like the cell ovalization and the variations in wall thickness and bond length were neglected.

4.1. *Initial response of a representative microsection*

In past investigations of problems exhibiting propagating instabilities [e.g. Kyriakides (1993); Papka and Kyriakides (1994)], significant insight into the underlying mechanisms of each problem was gained from analyzing smaller sections of the structure. We, thus, again first consider a honeycomb of infinite size which deforms uniformly and try to obtain its response to uniaxial loading from a representative microsection. The guidelines for selecting the microsection are that it yield accurately the initial stable response of the honeycomb and that it have the appropriate symmetries and degrees of freedom to enable simulation of the onset of the governing instability.

The microsection selected is drawn in bold line inside a larger section of undeformed honeycomb in Fig. 11. Its geometric characteristics correspond to the mean measured values of D, t and ϕ (see Table 2). Each of the six 60° sectors was discretized with six elements of the type described above. The following boundary conditions and symmetries were used. The horizontal and vertical displacements at point a were prescribed to be zero while the loading was applied by incrementally displacing the node at point d downward. The rotation and vertical displacement at point c were matched to the corresponding degrees of freedom at point e. The material is modeled through the elastic-powerlaw viscoplastic model described in the previous section with the material parameters given in Table 3.

† We are grateful to Hibbitt, Karlson and Sorenson Inc. for making ABAQUS available under academic licence.

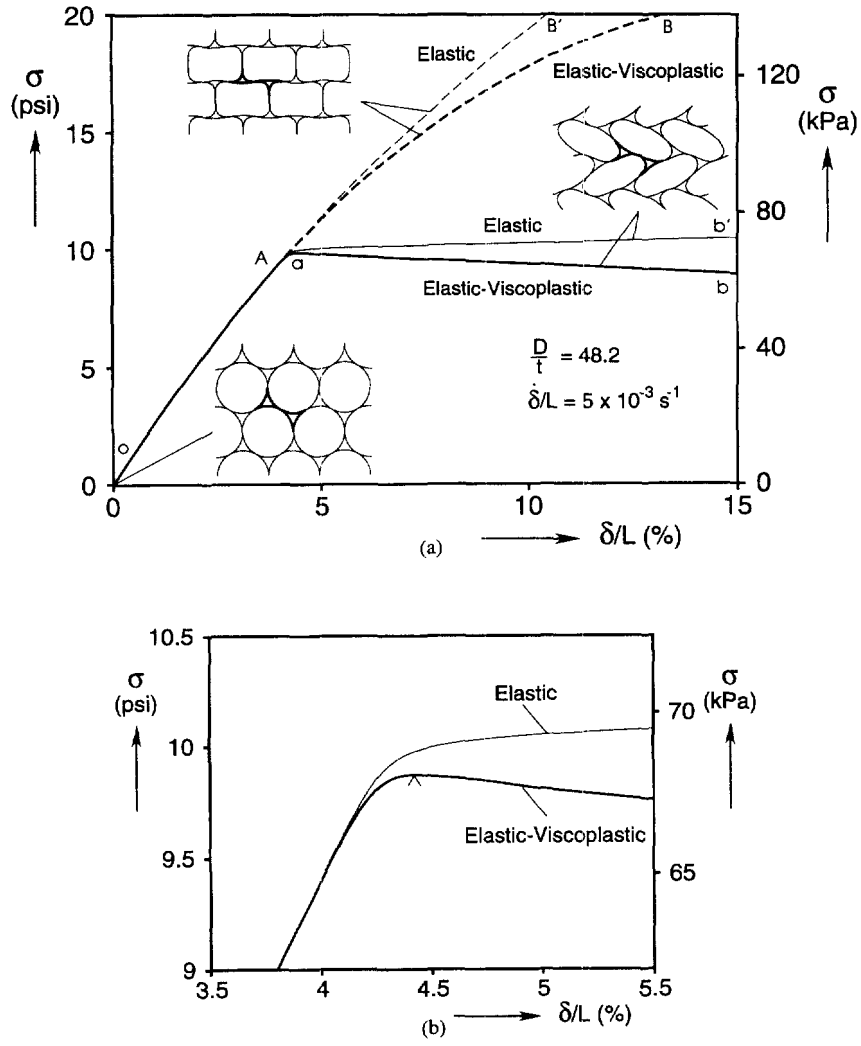

Fig. 12. (a) Calculated prebuckling and initial postbuckling response of elastic and elastic–viscoplastic microsections with $D/t = 48.2$; (b) expanded view of response in the neighborhood of the load maximum.

The microsection is loaded incrementally in a displacement-controlled fashion at a displacement rate of $\dot{\delta}/L = 5 \times 10^{-3}$. The average deformation is represented by δ/L ($\equiv \bar{\delta}$) where δ is the net shortening in the direction of the load and L is the original height of the microsection. The average stress (σ) required to induce the deformation is calculated by dividing the net vertical force by the initial cross-sectional area of the microsection.

The calculated σ–$\bar{\delta}$ response of the microsection is shown in Fig. 12(a) (bold solid line). Initially, the cells deform symmetrically about vertical axes passing through their centers as was observed in the experiments (see deformed configuration in upper left corner) and the response is relatively stiff and mildly nonlinear. The initial modulus, E^* is 272 psi (1.88 MPa—this result will be discussed in a separate section that follows). In the neighborhood of point a the microsection buckles into the shear-type mode shown in the deformed configuration in the upper right corner of the figure. The switch to the new branch was achieved smoothly by including a small initial geometric imperfection in the form of an asymmetry in the neighborhood of the full bond line of the microsection. This imperfection destabilizes the symmetric deformation when it is no longer energetically preferred. With the onset of unsymmetric deformation, a load maximum develops at $\sigma_c = 9.87$ psi (68.1 kPa) and $\bar{\delta}_c = 4.42\%$ and subsequently deformation grows with a decreasing stress (ab).

In order to understand the relative influence of geometric vis-à-vis material nonlinearities on the calculated response, we include in the same figure the corresponding

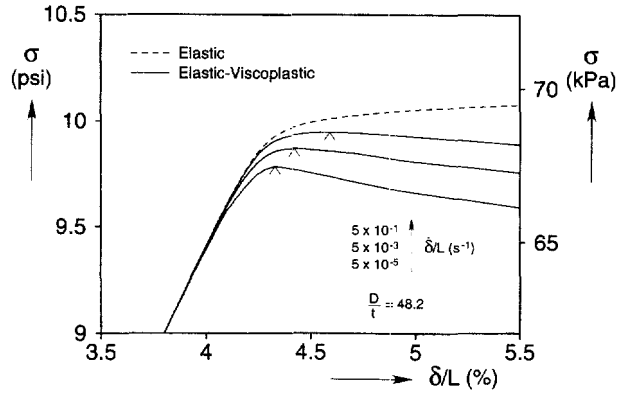

Fig. 13. Expanded views of microsection responses in the neighborhood of the load maximum for three different loading rates ($D/t = 48.2$).

response of a linearly elastic microsection (oab′). In the scale of this plot, the two responses seem indistinguishable up to point a when they both buckle into the unsymmetric mode at what seem to be essentially the same values of stress and strain. An expanded view of the two responses in the neighborhood of point a is shown in Fig. 12(b). The inelastic behavior causes the two responses to actually start deviating from each other before the limit load at a value of σ of approximately 9.5 psi (65.5 kPa).

The near coincidence of the two responses shows that for the geometric parameters of the present honeycomb, buckling is essentially an elastic event. In the neighborhood of a, viscoplastic effects start to influence the actual response. The elastic response maintains a small positive slope, whereas the inelastic one decays with $\bar{\delta}$.

Included in Fig. 12(a) are responses from elastic and inelastic microsections which were restrained to deform symmetrically. In both cases the responses remain monotonically increasing. The elastic response, oAB′, exhibits some modest nonlinearity which increases with stress. Inelasticity causes additional reduction in stiffness seen in oAB which starts to deviate from the elastic one again at a level of stress of approximately 9.5 psi (65.5 kPa). The additional softening of the response increases with stress.

The effect of rate of loading on the calculated response is illustrated in Fig. 13. Expanded views of the parts of the σ–$\bar{\delta}$ responses in the neighborhood of the onset of instability are shown for three displacement rates spanning five decades. As the rate of the test increases the response moves upwards and closer to that of the elastic material. Furthermore, the limit load increases, it occurs at a larger value of strain, and the slope of the post limit load response becomes less negative. The limit stresses for the three rates, in increasing order, were found to be 9.79, 9.87 and 9.95 psi (67.5, 68.1 and 68.6 kPa).

A second set of calculations was performed in which the wall thickness of the tubes was doubled ($t = 0.01136$ in—288 μm) while the values of all other parameters were kept the same. Results which correspond to those of the thinner honeycomb in Fig. 12(a) are shown in Fig. 14(a). In this case, the onset of instability is clearly much more affected by the inelastic characteristics of the material. As a result, the elastic and inelastic responses start to deviate from each other earlier and the difference between the buckling stresses and strains of the two materials are more pronounced. In addition, the postbuckling response of the inelastic honeycomb drops at a faster rate than the one in Fig. 12(a).

The effect of loading rate on the onset of instability is illustrated in Fig. 14(b). Increase in rate again has a stabilizing effect in that the limit stress and strain increase and the post-limit load response decays at a slower rate. The limit stresses for the three rates analyzed were found to be 67.9, 70.3 and 72.9 psi (468, 485 and 503 kPa). Thus, the percent increase in the limit stress for an increase in rate of two decades is significantly higher in this case than in the honeycomb with the thinner wall. The strains at the limit stresses were respectively 4.58, 4.68 and 4.78%.

For rate independent mechanical behavior, if a uniform deformation response of a large structure (*local response*), like the ones in Figs 12–14 is found to exhibit a limit load

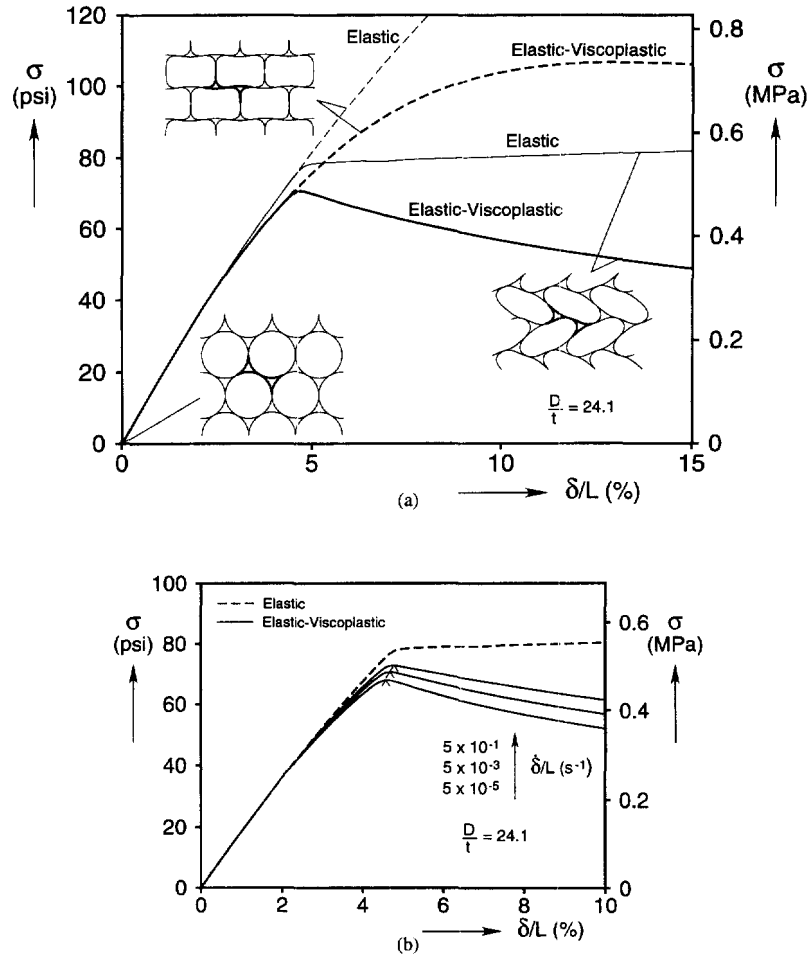

Fig. 14. (a) Calculated prebuckling and initial postbuckling response of elastic and elastic–viscoplastic microsections with $D/t = 24.1$; (b) microsection responses for three different loading rates.

instability, it is immediately concluded that uniform deformation will become unstable soon after the limit load. This is due to the fact that localized modes of deformation will be energetically preferred [see Kyriakides (1993)]. Strictly speaking, this conclusion cannot be made as categorically for rate dependent responses. However, for responses which are only mildly dependent on rate, such as the ones in Figs 12–14, a limit load instability in the local response is still an indicator that localized deformation may indeed be preferred even though the onset of localization may be delayed past the limit load.

4.2. *Simulation of crushing of a honeycomb specimen*

The remaining honeycomb properties of interest were calculated through full scale simulations of several of the crushing experiments. The geometry of the specimens analyzed was the same as that of the test specimens shown in Fig. 1 except that geometric imperfections were neglected (the model includes the partial cells at the edges of the specimens). The specimens were crushed between two rigid surfaces. One of the surfaces was held fixed while the second was prescribed a constant velocity ($\dot{\delta}$). Contact between the rigid walls and the honeycomb, as well as between the crushing walls of cells, was frictionless. The model had more than 27,500 variables (number of degrees of freedom + number of Lagrange multipliers). In addition, accurate modeling of viscoplastic behavior and contact between the walls of collapsing cells required that the prescribed velocity increments ($\Delta\delta$) be small. Thus, the calculations were computationally intensive and required that significant computer memory be available. In addition, a significant amount of disk space was required for post-processing the generated solution.

The position at which instability initiated was chosen by adding small couples on the walls of the central cells in a selected row of cells. This influences the resulting pattern of crushing but essentially has no other effect on the honeycomb properties of interest. In the results that follow, instability was initiated in approximately the same row in which it initiated in the corresponding experiment.

We first consider the results of the simulation of the experiment in Fig. 2 ($\dot{\delta}/L = 5 \times 10^{-3}$). The calculated σ–$\bar{\delta}$ response is plotted together with the corresponding experimental one in Fig. 15(a). A sequence of deformed configurations corresponding to the equilibrium points identified on the calculated response is shown in Fig. 15(b). Overall, the simulated response is seen to be in very good agreement with the experimental one. The deformation is initially symmetric about vertical axes through the centers of the cells and nearly uniform through the specimen [see configuration ① in Fig. 15(b)]. The initial modulus, E^*, measured over the same gage length as in the experiment, is 248 psi (1.71 MPa), that is, approximately 4% higher than the mean of the measured values in Table 1 and just less than 10% lower than the value yielded by the microsection. We point out that in specimens of relatively small size, like the ones used here, there exists a small gradient in deformation from the edge to the center. Thus, in both the experiments and the simulations, the initial slope of the overall σ–$\bar{\delta}$ response is lower than the value of E^* measured in the 2 in gage length at the center of the specimen (by approximately 20% in the analysis and 25% in the experiments).

The stable regime is terminated by a limit load instability at a stress of 9.48 psi (65.4 kPa) and a strain of approximately 6%. This value of σ_1 is 8.7% higher than the mean of

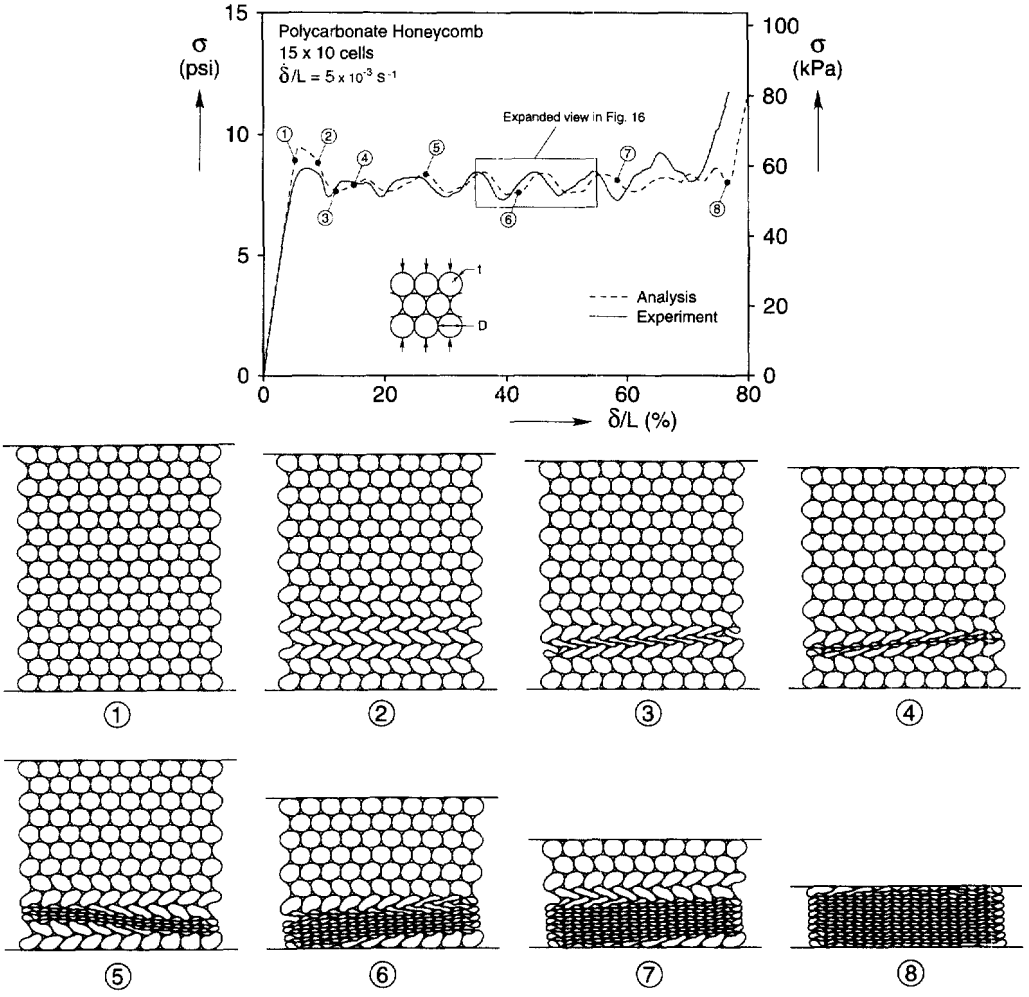

Fig. 15. (a) Comparison of measured and calculated force–displacement responses of a 15 × 10 cells honeycomb specimen loaded at an average strain rate of 5×10^{-3} s^{-1}; (b) sequence of calculated collapse configurations corresponding to response in Fig. 15(a).

the values measured. This difference can be attributed directly to the geometric imperfections present in the actual honeycomb but neglected in the model. The initiation stress is the variable most sensitive to geometric imperfections and some difference between predicted and measured values for this variable of this order of magnitude will persist in all of our results.

The instability is associated with the unsymmetric shear-type mode seen in the experiments (see configuration ②). With the onset of this instability deformation localizes in the 12th row of cells as illustrated in configuration 3. As this takes place the overall stress decays and, as a result, away from the zone of the collapse, growth of deformation has ceased and some unloading takes place. Soon after configuration ③, the walls of the collapsed row of cells come into contact (see ④) and local deformation is arrested. The deformation pattern is such that the collapsed zone is at a small inclination to the horizontal direction. The cells in rows 11 and 13, which have been significantly destablized by the collapse of their neighboring cells, are the next candidates for collapse. Rows 11 and 13 collapse first followed by rows 10 and 14. In the process, in order to maintain compatibility with the constraint provided by the end-plate, the inclination of the collapsed zone switched sign (see ⑤). By configuration ⑤, rows 11, 12 and 13 have collapsed. During the next stress valley the collapse of row 14 is completed and the inclination of the collapsed zone switches sign once more. Once the collapse of row 14 is completed, a single propagating collapse front remains which propagates upwards. A steady-state collapse pattern develops which continues up to the stress peak after point ⑦ on the response. Each stress undulation corresponds to the collapse of two neighboring rows. Collapse of rows 1 and 15 is influenced by the constraints of the end-plates and is somewhat less regular ($65\% < \delta/L < 77\%$). By configuration ⑧, all cells have collapsed, the material is densified and the response takes a sharp upturn.

The average value of the calculated propagation stress (σ_P) is 7.99 psi (55.1 kPa) which compares with a value of 8.0 psi (55.2 kPa) for the experiment in Fig. 15(a) (the mean value of σ_P from five experiments was 8.06 psi—55.6 kPa). The number of stress undulations on the calculated stress plateau, their locations and their amplitude are also in good agreement with those of the experiment (the amplitude of steady-state undulations of the calculated response is 0.37 psi—2.55 kPa—and of the corresponding experimental one is 0.52 psi—3.6 kPa). The two responses differ somewhat for $\delta/L > 60\%$ primarily because of differences in the crushing of the cells near the ends of the two specimens. This is due to the fact that in the experiment, geometric imperfections play a significant role in the order in which the last few cells collapse. For the same reason, densification is somewhat delayed in the analysis and thus the extent of the plateau ($\Delta\varepsilon_P$) is 70.7% compared to the measured value of 63.1%.

In order to elucidate the evolution of events during one period of the stress undulations, the part of the response in Fig. 15(a) inside the construction box is drawn expanded in Fig. 16. Ten deformed configurations (the top three rows were truncated for clarity), corresponding to the equilibrium points identified on the response, are shown in the same figure. As a reference, configuration ① in this figure corresponds to configuration ⑥ in Fig. 15. Both represent an equilibrium point in the fourth stress valley. In this configuration, cell row 7 is seen to have developed the shear-type deformation with a strong gradient from right to left. In configurations ② to ⑤, row 7 is seen to gradually collapse. In ⑤, the RHS of this row is totally collapsed and the LHS is severely deformed. Somewhere between equilibria ④ and ⑤ the collapse starts seeping to the row above (row 6). In configuration ⑤, the deformation in row 6 develops a gradient with the LHS being more severely deformed than the RHS. In configurations ⑥ to ⑩, row 6 is seen to gradually collapse from left to right while the stress gradually decreases down to a new valley. By configuration ⑩ the RHS of row 5 has been destablized and it starts to collapse while the overall stress increases.

In summary, each stress undulation, from valley to valley, represents the progressive right-to-left and left-to-right collapse of two rows of cells. As a result, the responses of 15 cell specimens tested had seven stress peaks and valleys (a few exceptions to this were observed due to unusual geometric imperfections). Specimens with more rows of cells have

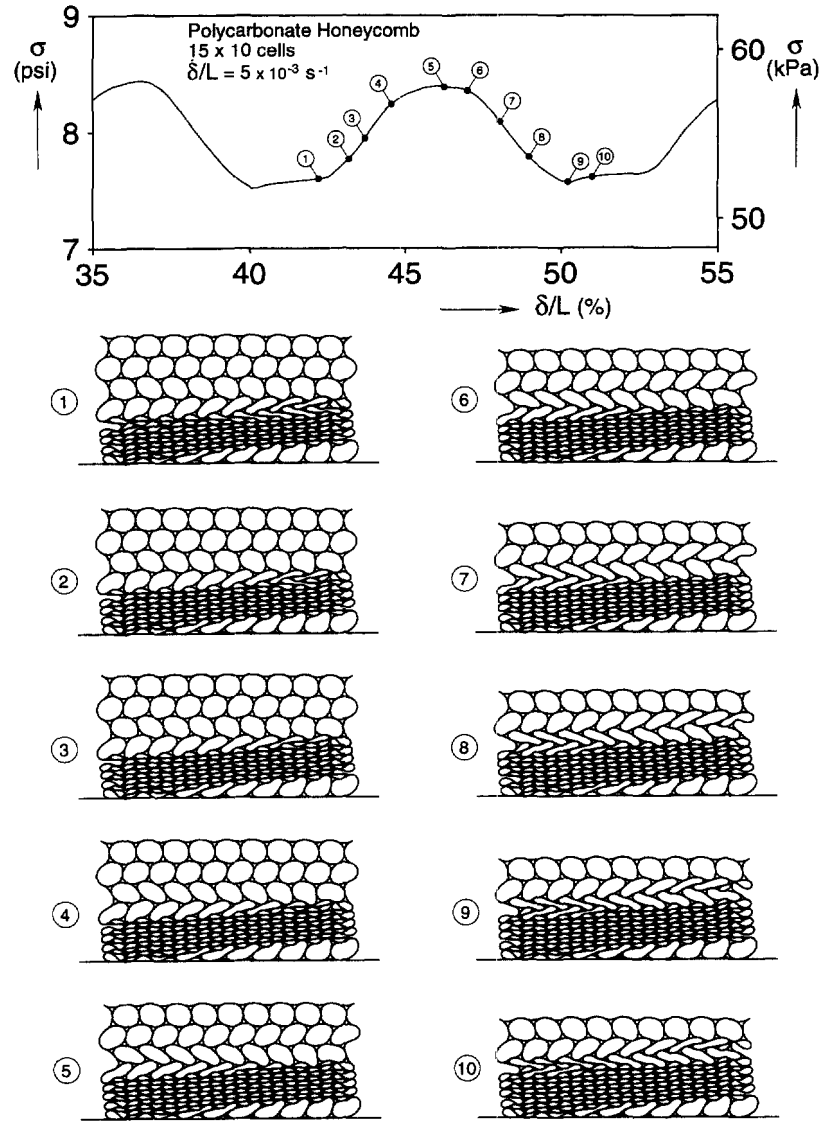

Fig. 16. Sequence of deformed configurations corresponding to one stress undulation in plateau region of response.

a proportionate number of more stress peaks. This is illustrated in the experimental response in Fig. 17 which came from a specimen with 21 rows by 14 columns of cells. The number of stress undulations is now 10 and, as a result, their period (measured by the normalized scale of δ/L) decreases proportionately. Interestingly, the evolution of events described and the characteristics of the undulations do not change with specimen width.

When developing the elastic–viscoplastic constitutive model used in this analysis, it was pointed out that localization of deformation and the subsequent propagation of collapse through the specimen place special demands on the model due to the large fluctuations in local strain rate. Having completed this numerical simulation, it is instructive to use the results to illustrate this point. Figures 18(c) and (d) show the strain rates ($\dot{\varepsilon}$), experienced at particular points in cells A and B identified in Fig. 18(a), plotted against the net shortening of the specimen. The point analyzed in each cell is identified in Fig. 18(b). Cell A belongs to the 12th row of cells where localization is initiated. Cell B is close enough to the initiation site to also be affected by the onset of the instability. The initial strain rate is seen to be constant in both cells. This corresponds to the stable part of the response. The strain rate in both cells starts to increase just before the global stress maximum. With the onset of the instability the strain rate in the two cells continues to increase due to the additional bending

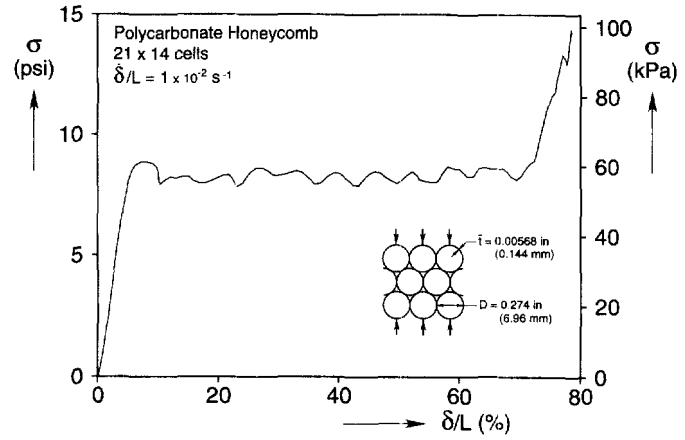

Fig. 17. Measured force–displacement response of crushing of a 21 × 14 cells honeycomb specimen.

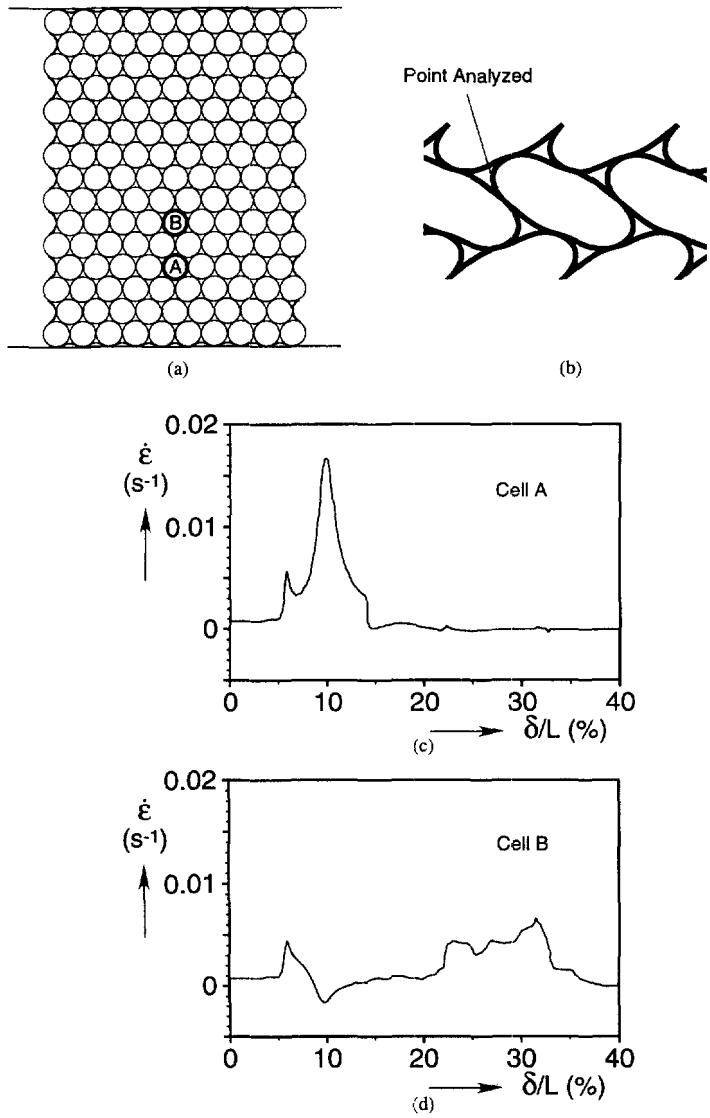

Fig. 18. Strain rate history at material points within crushed honeycomb specimen: (a) location of cells in specimen where strain rate was monitored; (b) location of point analyzed in cells A and B; (c) strain rate at predefined point in cell A vs average crushing strain; (d) strain rate at predefined point in cell B vs average crushing strain.

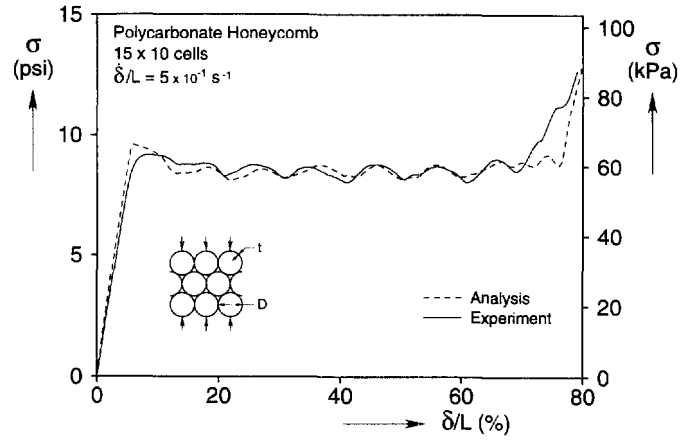

Fig. 19. Comparison of measured and calculated force–displacement responses of a 15×10 cells honeycomb specimen loaded at an average strain rate of $5 \times 10^{-1}\ s^{-1}$.

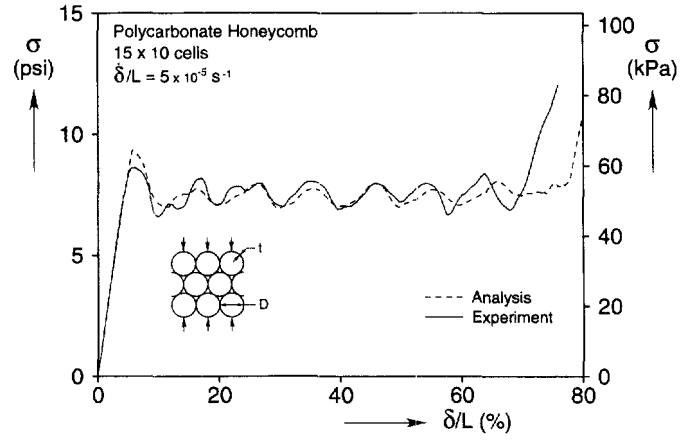

Fig. 20. Comparison of measured and calculated force–displacement responses of a 15×10 cells honeycomb specimen loaded at an average strain rate of $5 \times 10^{-5}\ s^{-1}$.

deformation associated with the shear type deformation. Since the deformation is localized in the neighborhood of the cells, unloading of cells away from this zone also contributes to the local increase in rate. The strain rate peaks at $\delta/L \approx 5.9\%$ and then starts to decrease because the switch to the shear mode is essentially completed. At $\delta/L \approx 6.8\%$ the rate in cell A starts to increase once more as collapse starts to be limited to row 12. The rate in A peaks at $\delta/L \approx 10\%$ and, subsequently, it decreases down to zero due to local arrest of deformation. The rate in cell B has also decreased to zero, but it picks up again when its turn to collapse comes at approximately $\delta/L \approx 22\%$. Collapse is completed just after δ/L of 34%. Because in this case at least two rows of cells were collapsing simultaneously and since additional deformation from unloading was no longer contributing to the local deformation, cell B never reached as high a strain rate as cell A.

4.3. *Simulation of honeycomb crushing at different end-displacement rates*

Full scale crushing simulations, similar to the one described above, were conducted for specimens of the same geometry loaded at end-displacement rates two decades lower ($\dot{\delta}/L = 5 \times 10^{-5}$) and two decades higher ($\dot{\delta}/L = 5 \times 10^{-1}$) than the rate of the simulation in Fig. 15. The calculated response for the faster rate is shown in Fig. 19 and for the slower rate in Fig. 20. A corresponding experimental response is included in each figure for comparison. The calculated and measured responses are seen to be in good agreement in both figures. The major parameters of interest extracted from the calculated responses are

Table 4. Predicted values of honeycomb major compressive mechanical properties

$\dot{\delta}/L$ s^{-1}	E^* psi (MPa)	σ_I psi (kPa)	σ_P psi (kPa)	$\Delta\varepsilon_P$ (%)	$\Delta\sigma_a$ psi (kPa)
5×10^{-5}	248 (1.71)	9.35 (64.5)	7.48 (51.6)	70	0.43 (2.97)
5×10^{-3}	248 (1.71)	9.48 (65.4)	7.99 (55.1)	70.7	0.37 (2.55)
5×10^{-1}	248 (1.71)	9.59 (66.1)	8.62 (59.4)	69.9	0.23 (1.59)

listed in Table 4. The three predicted responses are also plotted together in Fig. 21 for comparison.

The calculated initial elastic modulus of the honeycomb is the same for all rates because elastic deformations were assumed to be rate independent. The elastic modulus measured (using the same gage length—see Table 1) exhibited a small increase with rate but it was too small to warrant implementation of a more complex material model. The initiation stress exhibits a small increase with rate of the same order as that in Fig. 13. The initiation stresses are a bit higher than those measured for the reason already given. The average propagation stress for the slowest rate was 7.48 psi (51.6 kPa) which compares with 7.53 psi (51.9 kPa) for the experiment (mean value of experiments 7.50 psi (51.7 kPa). For the fastest rate the calculated value was 8.62 psi (59.4 kPa) and the measured 8.54 psi (58.9 kPa) (the mean value of the experiments was 8.63 psi—59.5 kPa). Thus, this variable is predicted with very good accuracy for all cases. For a more global comparison between experimental and predicted values of σ_I and σ_P, the values from the three calculated responses are included in the plot of all experimental results in Fig. 5. The calculated values of σ_P are seen to be in excellent agreement with the measured values whereas the calculated values of σ_I are consistently higher than those measured due to the absence of geometric imperfections in the model.

The extents of the stress plateaus are not affected by rate as was the case in the experiments. However, the calculated values for $\Delta\varepsilon_P$ are approximately 70% whereas the measured values were approximately 63%. The reason for this difference is that in the experiments, upon reaching the last stress valley, a few cells remained uncrushed as they required a higher value of stress to collapse. They collapsed during the rising part of the response of the densified material. As a result, its initial slope is lower than the slope of the corresponding calculated response. If this small difference is accounted for, then the calculated and measured energy absorption capacities are in excellent agreement.

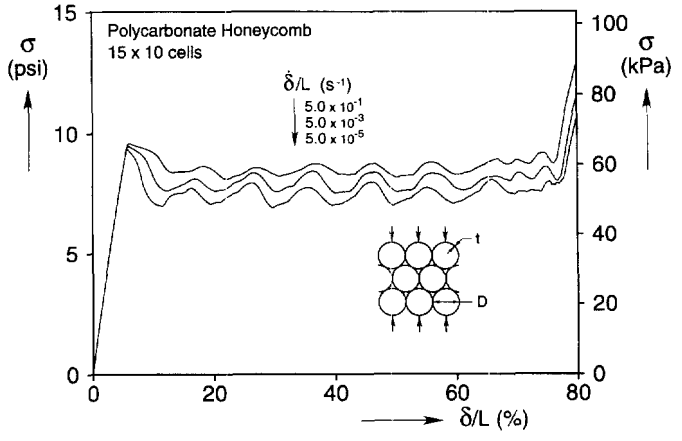

Fig. 21. Comparison of calculated force–displacement responses of 15 × 10 cells honeycomb specimens crushed at three different average strain rates.

The number, locations, and amplitudes of the stress undulations are, in the main, in good agreement with those of the experiments for the two new cases as well. Some minor differences between the measured and predicted undulations occur for all three cases close to the ends of the plateaus for the reason given above. The amplitudes of the undulations (under $\Delta\sigma_a$ in Table 4) are seen in Fig. 21 to decrease as the rate is increased. The undulations are somewhat more regular in the simulation and their amplitudes exhibit less variation than those of the measured responses. However, if we compare the mean values of $\Delta\sigma_a$ from the measured and predicted responses, the trend of $\Delta\sigma_a$ to decrease as the rate is increased is found to be quantitatively similar.

4.4. *Honeycomb elastic modulus*

The predictions of the initial elastic modulus of the honeycomb exhibited some interesting characteristics worth addressing on their own. In Section 4.2. it was mentioned that the elastic modulus predicted by the full simulation of a compression test of a 15×10 cell specimen, was 248 psi (1.71 MPa). This compared with an average measured value of 237 psi (1.63 MPa). Both of these values were measured in a 2 in gage length in the center of the specimen. By contrast, if based on the overall displacement of the specimen the estimate of E^* was lower by approximately 20% in the analysis and by 25% in the experiments. These differences are partly due to end effects, but also to a small gradient in deformation from the edge to the center of the specimen. The differences point to the potential influence of the method of measurement on the accuracy of this value.

The elastic modulus of an infinitely large section of the material is represented by the value yielded by compression of the micromodel in Figs 11 and 12 which yielded a value of 272 psi (1.88 MPa) for E^*. The same quantity was evaluated analytically using the extensional analysis outlined in Appendix A applied to cells of finite bond line. This analysis yielded a honeycomb modulus of 268 psi (1.84 MPa), that is very close to the value predicted numerically using the micromodel. Interestingly, when the size of the full scale model shown in Fig. 1 was increased to 35×25 cells, the value of the elastic modulus in the center increased to 263 psi (1.81 MPa), which is much closer to that of the two values involving representative cells. A similar increase in modulus as the specimen size increased was also observed in the experiments. These observations illustrate the sensitivity of the initial modulus to the size of the specimen. The free edges on the sides of finite size specimens like the one in Fig. 1 and the edge effects due to contact with the rigid plates at the upper and lower ends, affect the deformation. Thus, the size of the specimen must be many times larger than the size of the cell before these effects are dampened out in the central part of the specimen. By contrast, as reported earlier, other mechanical properties of the honeycomb such as σ_I, σ_P and $\Delta\varepsilon_P$ were found to be much less sensitive to specimen size.

The elastic modulus of such honeycombs can also be calculated analytically. In Appendix A we summarize analytical results for the simplest case in which the honeycomb cells are assumed to be bonded at single points. Reducing the bond length to a point reduces the stiffness of the honeycomb. For the case discussed above, the initial modulus of a honeycomb with extensional cells was predicted to be 222 psi (1.53 MPa). By contrast, the equivalent inextensional prediction was 2.7% higher. The difference between extensional and inextensional kinematics used in such calculations increases for honeycombs with higher density ratios (see Fig. A2).

5. SUMMARY AND CONCLUSIONS

It has been demonstrated experimentally that the compressive response of a polycarbonate honeycomb with circular cells is characterized by three regimes. At small strains the honeycomb deforms elastically. The deformation of each cell is symmetric about an axis through its center and deformation through the specimen is uniform (nearly). This is terminated by an instability involving a shear-type mode. Deformation soon localizes into a narrow zone a few rows of cells wide crossing the specimen. Deformation grows in this zone while the overall load drops and away from it the material unloads. Local deformation is arrested when the walls of the collapsing cells come into contact. Under displacement

controlled loading, collapse spreads through the rest of the specimen in a nearly steady-state fashion producing a stress plateau. During this phase of the deformation, the propagating front of the collapse was found to involve essentially two rows of cells. Collapse of each row was found to start on one side of the specimen and to gradually progress across to the other while at the same time the neighboring row was destabilized due to seepage of deformation into it. Each pair of rows produced a small but finite stress undulation on the stress plateau. The stress plateau is terminated when all rows of cells collapse. In the final deformation regime the specimen regains stiffness due to the densification suffered by the material. The stress required to initiate the instability and, more strongly, the stress at which it propagates were found to increase as the rate of crushing was increased due to the rate dependence of the polycarbonate base material.

The events observed in the experiments were simulated numerically using appropriately nonlinear kinematics and by proper treatment of the contact between the walls of collapsing cells. The cells were assumed to be perfectly circular and close-packed with diameter and thickness corresponding to the mean values of these parameters measured in the honeycombs tested. An important feature of the analysis was the inclusion of finite length bond lines between the cells which has a stiffening effect on the honeycomb response. The mechanical behavior of the polymeric base material was modeled as elastic-powerlaw viscoplastic. The constitutive model was calibrated to stress–strain responses measured at strain rates spanning six decades. It was further tested to ensure it could perform well in uniaxial histories involving loading-unloading with sudden changes in strain rate and found to perform very well.

The initial stable part of the response as well as the onset of instability were shown to be accurately predicted by assuming the deformation in the honeycomb to be uniform which allows limiting consideration to a representative micromodel. In addition, results from three full scale numerical simulations of experiments on 15×10 cells specimens, crushed at three different end-displacement rates, were presented. The three simulations were found in general to be in very good agreement with the corresponding experimental results. The calculated values of elastic modulus, propagation stress and energy absorption capacity of the material were in excellent agreement with the measured values. The rate dependence of the responses was reproduced with accuracy. Secondary features of the responses, such as the stress undulations on the stress plateau, were also reproduced well. The calculated initiation stress was, in general, somewhat higher than the values measured primarily due to the assumed perfect geometry of the cells. This small discrepancy can be easily corrected by including actual cell imperfections in the model. In conclusion, the results of this study demonstrate that if the geometric and material characteristics of cellular materials are established and modeled appropriately, the compressive properties of such materials can be predicted with high accuracy.

Acknowledgements—The financial support of the Air Force Office of Scientific Research under grant number F49620-95-1-0154 is acknowledged with thanks. The authors wish also to thank Plascore for their cooperation in designing and constructing the honeycomb used in the experiments.

REFERENCES

Ashby, M. F. (1983) The mechanical properties of cellular solids. *Metallurgical Transactions*, **14A**, 1755–1769.

Gibson, L. J. and Ashby, M. F. (1982) The mechanics of three dimensional cellular materials. *Proceedings of the Royal Society of London*, **A382**, 43–59.

Gibson, L. J. and Ashby, M. F. (1988) *Cellular Solids: Structure and Properties*. Pergamon Press, Oxford.

Gibson, L. J., Ashby, M. F., Schajer, G. S. and Robertson, C. I. (1982) The mechanics of two-dimensional cellular materials. *Proceedings of the Royal Society of London*, **A382**, 25–42.

Green, S. J., Schierloh, F. L., Perkins, R. D. and Babcock, S. G. (1969) High-velocity deformation properties of polyurethane foams. *Experimental Mechanics*, **9**, 103–109.

Hinckley, W. M. and Yang, J. C. S. (1975) Analysis of rigid polyurethane foam as a shock mitigator. *Experimental Mechanics*, **15**, 177–183.

Klintworth, J. W. and Stronge, W. J. (1988) Elasto-plastic yield limits and deformation laws for transversely crushed honeycombs. *International Journal of Mechanical Sciences*, **30**, 273–292.

Kyriakides, S. (1993) Propagating instabilities in structures. In *Advances in Applied Mechanics*, Vol. 30, ed. J. W. Hutchinson and T. Y. Wu, pp. 67–189. Academic Press, Boston.

Nadai, A. (1950) *Theory of Flow and Fracture of Solids*, Vol. I, 2nd end. McGraw-Hill, New York.

Papka, S. D. and Kyriakides, S. (1994) In-plane compressive response and crushing of honeycomb. *Journal of Mechanics and Physics of Solids*, **42,** 1499–1532.
Patel, M. R. and Finnie, I. (1970) Structural features and mechanical properties of rigid cellular plastics. *Journal of Materials*, **5,** 909–932.
Peirce, S. D., Shih, C. F. and Needleman, A. (1984) A tangent modulus method for rate dependent solids. *Computers and Structures*, **18,** 875–887.
Prakash, O., Bichebois, P., Brechet, Y., Louchet, F. and Embury, J. D. (1996) A note on the deformation behaviour of two-dimensional model cellular structures. *Philosophical Magazine*, **A73,** 739–751.
Richardson, M. O. W. and Nandra, D. S. (1985) Load-deflection analyses of shock mitigating polyurethene-silicone foams. *Cellular Polymers*, **4,** 445–462.
Shaw, M. C. and Sata, T. (1966) The plastic behavior of cellular materials. *International Journal of Mechanical Sciences*, **8,** 469–478.
Sherwood, J. A. and Frost, C. C. (1991) Constitutive modeling and simulation of energy absorbing polyurethane foam under impact loading. *Plastics and Plastics Composites: Material Properties, Part Performance and Process Simulation*, MD-Vol. 29, ed. V. J. Stokes, pp. 347–370.
Shim, V. P.-W. and Stronge, W. J. (1986) Lateral crushing of tightly packed arrays of thin-walled tubes. *International Journal of Mechanical Scineces*, **28,** 709–728.
Shim, V. P.-W., Yap, K. Y. and Stronge, W. J. (1992) Effects of nonhomogeneity, cell damage and strain-rate on impact crushing of a strain-softening cellular chain. *International Journal of Impact Engineering*, **12,** 585–602.
Triantafyllidis, N. and Schraard, M. W. (1997) Onset of failure in honeycomb under arbitrary inplane loading. *Journal of Mechanics and Physics of Solids* (to appear).
Tugcu, P. and Neale, K. W. (1987) Analysis of plane strain neck propagation in viscoplastic polymeric films. *International Journal of Mechanical Sciences*, **29,** 793–805.
Tugcu, P. and Neale, K. W. (1988) Analysis of neck propagation in polymeric fibres including the effects of viscoplasticity. *ASME Journal of Engineering Materials and Technology*, **110,** 395–400.
Warren, W. E. and Kraynik, A. M. (1987) Foam mechanics: the linear elastic response of two-dimensional spatially periodic cellular materials. *Mechanics of Materials*, **6,** 27–37.
Warren, W. E., Kraynik, A. M. and Stone, C. (1989) A constitutive model for two-dimensional nonlinear elastic foams. *Journal of Mechanics and Physics of Solids*, **37,** 717–733.
Zhang, J. and Ashby, M. F. (1992) Buckling of honeycombs under in-plane biaxial stresses. *International Journal of Mechanical Sciences*, **34,** 491–509.

APPENDIX A

Analytical expressions for the elastic modulus of the honeycomb

The initial elastic modulus of the honeycomb can be calculated analytically using linear kinematics. For simplicity, we consider a honeycomb with an hexagonal array of circular cells of radius R $(=D/2)$ and wall thickness t bonded to each other only at points. Here we are interested in cell deformations symmetric about an axis parallel to the line of loading passing through the cell center. As a result, it is sufficient to analyze just the representative section drawn in bold line in Fig. A1. The free body diagram shown has incorporated in it simplifications dictated by the various symmetries of the problem (consider the forces and moments to be the values per unit depth). For cells with high R/t values, membrane deformations can be neglected and then the strain energy of this section is

$$U = 2\left\{\int_0^{\pi/6} \frac{[M_1(\theta)]^2}{2\hat{D}} R\,\mathrm{d}\theta + \int_0^{\pi/3} \frac{[M_2(\theta)]^2}{2\hat{D}} R\,\mathrm{d}\theta\right\} \tag{A1}$$

where $M_1(\theta)$ and $M_2(\theta)$ are the moment intensity distributions in sectors ab and bc respectively, θ is the polar angle,

$$\hat{D} = \frac{E' t^3}{12} \quad \text{and} \quad E' = \frac{E}{(1-\nu^2)}. \tag{A2}$$

The three redundancies of the problem can be evaluated from

$$\frac{\partial U}{\partial M_a} = 0, \quad \frac{\partial U}{\partial H} = 0 \quad \text{and} \quad \frac{\partial U}{\partial P} = \delta. \tag{A3}$$

From the resultant relationship between P and δ the equivalent modulus of the honeycomb, E^*, is given by

$$E^* = 2\frac{P}{\delta}\cos\left(\frac{\pi}{6}\right) \tag{A4}$$

which results in

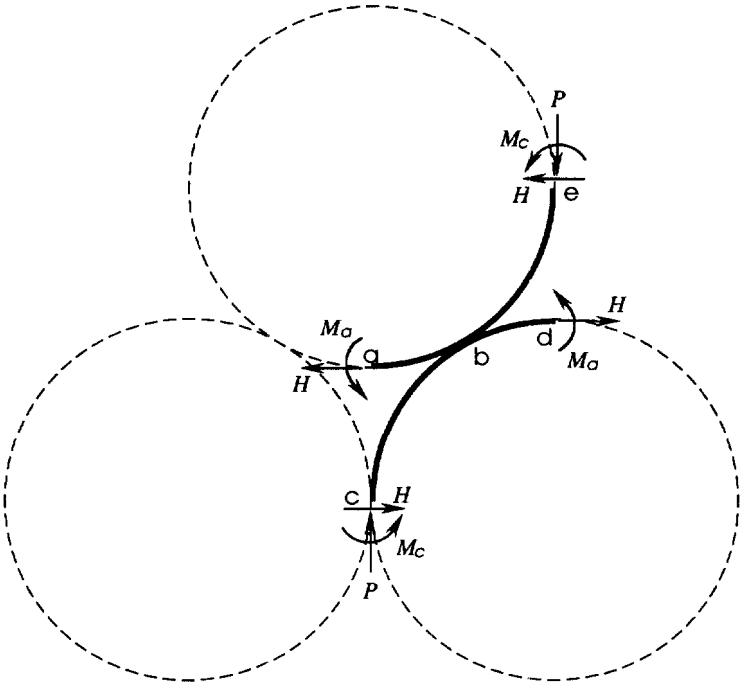

Fig. A1. Free body diagram of section used to calculate the initial elastic modulus of the honeycomb.

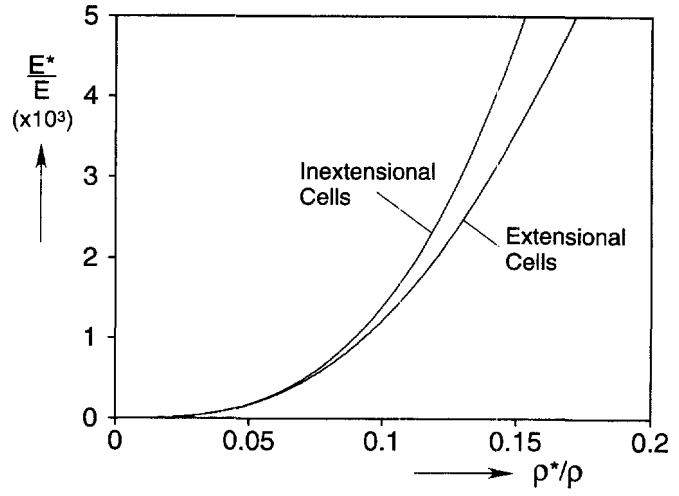

Fig. A2. Relative modulus vs relative density predicted by inextensional and extensional cell models.

$$\frac{E^*}{E'} \approx 8.329\left(\frac{t}{R}\right)^3. \tag{A5}$$

For cells with lower E^*/E values, eqn (A5) overestimates the modulus. An improved estimate can be obtained in a similar fashion by including the contribution of membrane effects in the strain energy which then becomes

$$U = \int_0^{\pi/6} 2\left\{\frac{[N_1(\theta)]^2}{2\hat{C}} + \frac{[M_1(\theta)]^2}{2\hat{D}}\right\} R\,\mathrm{d}\theta + \int_0^{\pi/3} 2\left\{\frac{[N_2(\theta)]^2}{2\hat{C}} + \frac{[M_2(\theta)]^2}{2\hat{D}}\right\} R\,\mathrm{d}\theta \tag{A6}$$

where $N_1(\theta)$ and $N_2(\theta)$ are the stress intensity distributions in sectors ab and bc, respectively, and

$$\hat{C} = E't. \tag{A7}$$

Equation (A6) yields an expression for E^*/E which depends on $(t/R)^3$ as well as (t/R). The values of E^*/E predicted by these extensional and inextensional analyses are plotted as a function of the density ratio ρ^*/ρ in Fig. A2. For $\rho^*/\rho < 0.08$ the inextensional analysis is quite accurate. For high density ratios it becomes progressively less accurate. Similar calculations were performed for cells with finite bond lines. The resultant expressions are rather complicated and will not be quoted here.